

Theory of superdiffusive spin transport in noncollinear magnetic multilayers

Pavel Baláz^{1,*}, Maciej Zwierzycki², Francesco Cosco³, Karel Carva⁴, Pablo Maldonado³, and Peter M. Oppeneer³

¹*FZU—Institute of Physics of the Czech Academy of Sciences, Na Slovance 1999/2, 182 21 Prague 8, Czech Republic*

²*Institute of Molecular Physics, Polish Academy of Sciences, Smoluchowskiego 17, 60-179 Poznań, Poland*

³*Department of Physics and Astronomy, Uppsala University, Box 516, SE-75120 Uppsala, Sweden*

⁴*Faculty of Mathematics and Physics, Department of Condensed Matter Physics, Charles University, Ke Karlovu 5, CZ 121 16 Prague, Czech Republic*



(Received 30 November 2022; revised 5 April 2023; accepted 5 April 2023; published 12 May 2023)

Ultrafast demagnetization induced by femtosecond laser pulses in thin metallic layers is caused by the outflow of spin-polarized hot-electron currents describable by the superdiffusive transport model. These laser-generated spin currents can cross the interface into another magnetic layer and give rise to magnetization dynamics in magnetic spin valves with noncollinear magnetizations. To describe ultrafast transport and spin dynamics in such nanostructures, we develop here the superdiffusive theory for general noncollinear magnetic multilayers. Specifically, we introduce an Al/Ni/Ru/Fe/Ru multilayer system with noncollinear Ni and Fe magnetic moments and analyze how the ultrafast demagnetization and spin-transfer torque depend on the noncollinearity. We employ *ab initio* calculations to compute the spin- and energy-dependent transmissions of hot electrons at the interfaces of the multilayer. Taking into account multiple electron scattering at interfaces and spin mixing in the spacer layer, we find that the laser-induced demagnetization of the Ni layer and the magnetization change of the Fe layer strongly depend on the angle between their magnetizations. Similarly, the spin-transfer torques on the Ni and Fe layers and the total spin momentum absorbed in the Ni and Fe layer are found to vary markedly with the amount of noncollinearity. These results suggest that by changing the amount of noncollinearity in magnetic multilayers, one can efficiently control the hot-electron spin transport, which may open a way toward achieving fast, laser-driven spintronic devices.

DOI: [10.1103/PhysRevB.107.174418](https://doi.org/10.1103/PhysRevB.107.174418)

I. INTRODUCTION

Fast and energy-efficient control of the magnetic configuration of nanostructures is a fundamental requirement for practical spintronic devices. Ever since the discovery of the spin-transfer torque (STT) by Slonczewski [1] and Berger [2] in 1996, the STT has been seen as a major candidate for achieving this goal. The main obstacle for widespread application of STT is the high current densities that are required for effectuating the change of magnetization alignment. One possible way of addressing this problem is to use the so-called spin-orbit torque [3–5], a torque variant where the pure spin current penetrating into the magnetic layer is generated by the spin Hall effect [6] or related effects such as the Rashba-Edelstein effect originating microscopically from strong spin-orbit coupling [7].

Another possibility to manipulate spins has emerged from the line of research which started with the breakthrough experiment by Beaurepaire *et al.* [8], who observed ultrafast demagnetization of a nickel thin film after exposing it to a femtosecond laser pulse. The intriguing possibility of subpicosecond-scale manipulation of the magnetic order inspired a number of follow-up studies, both experimental and theoretical [9]. However, it took more than 10 years until

research in the field of ultrafast laser-induced magnetization processes had been combined with spintronics leading to discoveries of optical spin-transfer torque [10] and optical spin-orbit torque [11]. The importance of spin-transfer effects in the demagnetization of metallic multilayers has been observed by Malinowski *et al.* [12]. The demagnetization in metallic structures was attributed to the spin transfer of laser-excited hot electrons moving across the sample. Since electron velocities and lifetimes in magnetic metals are strongly spin dependent, electronic motion leads to fast spin currents contributing to ultrafast demagnetization. Theoretically, this process has been described by the superdiffusive spin-dependent transport model of Battiato *et al.* [13,14], explained in more detail in Sec. II A. The important role of spin currents in ultrafast demagnetization is supported by a number of experimental observations [15–25].

Additional support for the nonthermal hot-electron spin-current picture comes from Ref. [26], where the effect of a femtosecond laser pulse has been studied in magnetic trilayers, consisting of two ferromagnetic layers separated by a nonmagnetic spacer. When the magnetizations of the ferromagnetic layers are collinearly aligned and one of them is illuminated by the laser pulse, its ultrafast demagnetization is followed by the subsequent transient increase in the magnetization of the second layer. However, in the antiparallel configuration the same procedure leads to a decrease in the second layer's magnetization. This effect can be readily

*balaz@fzu.cz

understood in terms of the hot-electron spin current being generated in the first layer and carrying the spin polarization aligned with this layer into the second one. Moreover, the results were shown to be in good agreement with the superdiffusive transport model. On the other hand, Eschenlohr *et al.* [27] have inspected the same kind of trilayer using *L*-edge x-ray magnetic spectroscopy and found no enhancement of magnetization.

The discrepancy between experimental results calls for further development of the theoretical approach allowing for even more precise modeling of hot-electron transport in complex multilayered structures. In the current paper we discuss the following twofold improvement to the superdiffusive transport model: (i) the inclusion of a realistic, material-specific description of the scattering at the interfaces and (ii) the extension of the formalism to the case of noncollinear magnetic configurations.

Noncollinear magnetic alignments appear frequently, adding a novel aspect to ultrafast spin transport in magnetic nanostructures. For example, a number of recent experiments studied ultrafast demagnetization in multilayers combining a ferromagnet and Pt [28–30]. In the case of Co/Pt it is possible to achieve not only in-plane, but also out-of-plane magnetization orientation [30], which makes such system an interesting candidate for studies of the role of noncollinearity. Several recent experiments probed the ensuing magnetization dynamics in noncollinear magnetic multilayers [17,18,31–33].

The most significant manifestation of the optically induced spin currents in noncollinear magnetic multilayers or magnetic textures is the appearance of a STT leading to magnetization dynamics. To this end, a number of experiments focused on magnetic trilayers with noncollinear (usually perpendicular) magnetizations. These experimental observations [17,18,32,33] and theoretical models [34] suggest laser excitation of hot electrons in one magnetic layer can lead in quick succession to small-angle precession of the moment of the second magnetic layer, caused by the STT due to the spin current, even though both magnetic layers are separated and magnetically decoupled by a nonmagnetic spacer. Interestingly, experiments [32,35] and numerical simulations [36,37] have revealed that a spin current of hot electrons in noncollinear spin valves can trigger terahertz spin waves.

The interplay between the laser-induced spin currents and localized magnetization touches upon a central interest in ultrafast spintronics, having the potential to fulfill both requirements mentioned earlier in this section—speed and efficiency. The first characteristic results from the fundamentally different transport regime, distinct from the usual diffusive/Ohmic one, governing the propagation of the spin information across the system. The hot electrons propagate initially in nearly ballistic fashion, which means that their real velocity (Bloch velocity) is relevant, which is many orders of magnitude higher than the drift velocity characterizing the collective motion in diffusive systems. The efficiency follows from the cascade effect [13,14] where after the absorption of a single photon, the excited electron can, in subsequent scatterings, excite many more, multiplying thereby the number of particles carrying the spin information [14].

To describe laser-induced STT and magnetization dynamics in magnetic multilayers, we recently developed an

effective model for the STT induced by hot electrons in perpendicular noncollinear spin valves [34]. Moreover, by means of atomistic spin dynamics we have demonstrated the possibility of generation of terahertz spin waves in a magnetic film due to the superdiffusive STT exerted by hot electrons [37]. Later on, to describe arbitrary noncollinear magnetic textures like a domain wall, we generalized the superdiffusive transport model by including a spin rotation transformation [38] and predicted a high-speed shift of the domain wall center due to a femtosecond laser pulse. The model was also used to predict optimal spacer thickness to maximize the hot-electron spin current and an impressive agreement between these theoretical predictions and experiment has been observed [39].

As a further motivation, there is an ongoing effort to achieve magnetization reorientation into a desired direction by means of a light pulse. One example is the precession caused by the Zeeman interaction with the magnetic component of light, an effect best manifested in the terahertz range [40]. Another case is the laser-induced magnetization due to the inverse Faraday effect [41]. In both these cases an optical pulse will cause inevitable excitation of electrons in addition to the magnetization reorientation, and superdiffusive currents may thus occur. The resulting demagnetization and STT could help ease the switching; on the other hand, the loss of magnetization could unfortunately dominate over switching. It is therefore needed to provide the description of superdiffusion-related effects also for arbitrary angles reached during the switching process in order to describe the magnetization dynamics of such process completely. Interesting discoveries regarding magnetization dynamics in noncollinear structures with a chirality were made recently [42]. Noncollinear anti-ferromagnetic spin structures not restricted to perpendicular angles were also predicted to feature unusual properties of the current-induced STT, including a self-generated torque [43].

In the current paper, we study the hot-electron transport in the magnetic multilayer, namely, the Al/Ni/Ru/Fe/Ru structure also studied experimentally [16,26,27]. Using the superdiffusive transport model, we inspect the demagnetization as well as spin-transfer torques acting on the magnetic layers after the hot electrons are excited by a femtosecond laser pulse. In order to properly describe the transport through the interfaces, we employed the *ab initio* wave function matching (WFM) method [44,45] to calculate spin- and energy-dependent transmissions of hot electrons. Thus, the superdiffusive transport model allows us to account for multiple reflections of electrons from the interfaces together with bulk scattering of hot electrons. In the case of noncollinear magnetic configuration, spin mixing in the central nonmagnetic layer has to be taken into account. Since this layer is usually just a few atomic monolayers thick, we model the nonmagnetic spacer as a single interface between the magnetic layers allowing spin mixing of the hot electrons passing through it. In collinear magnetic configurations [17], we have shown that our assumption has just a minor effect on the results obtained by the superdiffusive transport model.

The importance of interface scattering is well established for the case of conventional Fermi-level spin transport [46,47]. Its effect on the process of ultrafast demagnetization in a ferromagnet/normal metal bilayer was recently studied independently, and found to be meaningful, in Ref. [48]

using an approach similar to that outlined in Secs. II A and II C.

The paper is organized as follows. In Sec. II A we present the main features of the spin-dependent superdiffusive transport model. The system for which the calculations are performed is described in Sec. II B and the method for calculating the scattering coefficients for interfaces is discussed in Sec. II C. In Sec. III we present our calculations of transmissions through the interlayer interfaces. The results for ultrafast demagnetization and spin-transfer torque in a noncollinear Ni/Ru/Fe trilayer are described in Secs. IV and V, respectively. We conclude in Sec. VI.

II. THEORY

A. The superdiffusive transport model

Laser pulses in relevant experiments provide photons with energies around 1.5 eV. Electrons excited by photons to energies in this range possess properties that differ significantly from those of electrons near the Fermi level. In the studied materials predominantly immobile d electrons are present near the Fermi level, while the excited ones may be rather of sp character. These sp electrons are characterized by higher velocities, hence, they behave as itinerant particles moving through the sample. The change of magnetization of a metallic layer due to the transport dynamics of these electrons has been described by the superdiffusive spin-dependent transport model [13,14]. We note that an alternative approach to describe the collision-rich motion of excited hot electrons in metallic layers has been developed on the basis of Boltzmann transport theory [49,50].

The superdiffusive transport model describes two spin channels, tagged as $\sigma \in \{\uparrow, \downarrow\}$, for the electronic transport. Each spin channel within a specific material is characterized by the hot-electron velocities, $v_\sigma(\epsilon)$, and lifetimes, $\tau_\sigma(\epsilon)$, which depend on the electron energy ϵ , and, in magnetic materials, on the spin σ as well. Calculation of these excited electron properties requires an adequate method; in our model we utilize results obtained within the GW + T approach [51,52]. Because of the distinct transport properties of the two spin channels, the current of hot electrons gets spin polarized in the magnetic layer. In addition, in the case of multilayers, spin filtering via multiple spin-dependent

transmissions and reflections at the interfaces further contributes to the spin polarization of the current [53].

The outflow of the spin-polarized current initiated by a laser pulse results in a loss of local magnetic momentum and demagnetization. Due to the high velocities of hot electrons, the demagnetization happens on a timescale of hundreds of femtoseconds [13]. Initially, the hot electrons' propagation is ballistic; however, due to the relaxation processes caused by electron scattering, it continuously changes its character. In about 500 fs up to 1 ps it develops into a purely diffusive one. In the time interval up to 500 fs, the transport proceeds in the superdiffusive regime [14].

Let us describe briefly the main features of the superdiffusive spin-dependent transport model formulated in Refs. [13,14], which revolves around the equation of motion for the hot-electron density $n_\sigma(\epsilon, z, t)$, with spin σ , energy ϵ , and position z ,

$$\frac{\partial n_\sigma(\epsilon, z, t)}{\partial t} + \frac{n_\sigma(\epsilon, z, t)}{\tau_\sigma(\epsilon, z)} = \left(-\frac{\partial}{\partial z} \hat{\phi} + \hat{I} \right) S_\sigma^{\text{eff}}(\epsilon, z, t), \quad (1)$$

where $\hat{\phi}$ is the flux operator which contains the dependence from the electrons' velocities and describes interlayer transmissions and reflections. Furthermore, $S_\sigma^{\text{eff}}(\epsilon, z, t)$ is an effective source term describing the laser-induced excitation of spin-polarized hot electrons and scattering events within the material (see the discussion below).

For practical calculations we adopt the discretized version of the formalism, described in Ref. [53], with the space divided into computational cells of width δz . Time and energy are also sampled in finite steps of δt and $\delta \epsilon$, respectively.

When treating the multilayers, one should include the possibility of scattering at the interlayer interfaces. It is convenient to formally treat each computational cell as an individual layer and its boundaries as interfaces characterized by specific transmission probabilities. Therefore, until the end of the current section, the term interface will refer to interfaces between the computational cells, even though only some of these correspond to actual interfaces between different metallic layers with nontrivial scattering coefficients.

Following Ref. [53], the solution of Eq. (1) on the discrete grid, averaged over the cell centered at z_i and omitting, for the sake of brevity, the energy index ϵ , can be written as

$$\begin{aligned} n_\sigma(z_i, t + \delta t) = & e^{-\delta t/\tau_\sigma(z_i)} n_\sigma(z_i, t) + S_\sigma^{\text{eff}}(z_i, t + \delta t) \\ & + \sum_{\sigma'} [\vec{T}_{\sigma, \sigma'}(z_i^-) \vec{\Phi}_{\sigma'}(z_i^-, t) + \overleftarrow{T}_{\sigma, \sigma'}(z_i^-) \overleftarrow{\Phi}_{\sigma'}(z_i^-, t) - \vec{T}_{\sigma, \sigma'}(z_i^+) \vec{\Phi}_{\sigma'}(z_i^+, t) - \overleftarrow{T}_{\sigma, \sigma'}(z_i^+) \overleftarrow{\Phi}_{\sigma'}(z_i^+, t)], \end{aligned} \quad (2)$$

where $z_i^\pm = z_i \pm \delta z/2$ are the positions of the left and right interface, respectively, for each cell centered at z_i . $\vec{\Phi}_\sigma(z_i^\pm, t)$ and $\overleftarrow{\Phi}_\sigma(z_i^\pm, t)$ are the fluxes of right- and left-moving particles with spin σ going through the interface z_i^\pm of the cell at time t . Each interface is characterized by energy-dependent transmissions of electrons moving to the right, $\vec{T}_{\sigma \sigma'}$, and to the left, $\overleftarrow{T}_{\sigma \sigma'}$, with σ and σ' indicating spin after and before

the transmission, respectively. Thus, the first term in the sum represents the incoming fluxes through the left interface of the cell, while the second term represents the outgoing fluxes through the left interface. In a similar fashion, the third term stands for the outgoing fluxes through the right interface, and the last term expresses the incoming fluxes through the right interface. The first two terms of Eq. (2) describe the variation of n_σ due to the spin relaxation and effective source,

respectively. The latter is made of two contributions, i.e.,

$$S_{\sigma}^{\text{eff}}(z, t + \delta t) = S_{\sigma}^{\text{ext}}(z, t + \delta t) + S_{\sigma}^{\text{p}}(z, t + \delta t), \quad (3)$$

where $S_{\sigma}^{\text{ext}}(z, t + \delta t)$ describes the excitation of hot electrons by the laser pulse, and $S_{\sigma}^{\text{p}}(z, t + \delta t)$ is the term describing the effects of scattering, mostly caused by electron-electron interactions, calculated as

$$S_{\sigma}^{\text{p}}(\epsilon, z, t + \delta t) = \sum_{\sigma'} \int_{\epsilon_{\text{Fermi}}}^{\epsilon_{\text{max}}} d\epsilon' n_{\sigma'}(\epsilon', z, t) \times p_{\sigma',\sigma}(\epsilon', \epsilon, z, t)(1 - e^{-\delta t/\tau_{\sigma'}(\epsilon', z, t)}), \quad (4)$$

where, in general, $p_{\sigma',\sigma}(\epsilon', \epsilon, z, t)$ is the probability that an electron at energy level ϵ' , between the Fermi energy ϵ_{Fermi} and the energy cutoff ϵ_{max} , and spin σ' will move to energy level ϵ with spin σ in the next time step, $t + \delta t$.

$$\begin{aligned} \vec{\Phi}_{\sigma}(z_i^+, t) &= \sum_{t_0=0}^t S_{\sigma}^{\text{eff}}(z_i, t_0) \psi_{\sigma}(z_i^+, t|z_i, t_0) + \sum_{\sigma'} [\vec{T}_{\sigma,\sigma'}(z_i^-) \vec{\Phi}_{\sigma'}(z_i^-, t) + \overleftarrow{R}_{\sigma,\sigma'}(z_i^-) \overleftarrow{\Phi}_{\sigma'}(z_i^-, t)], \\ \overleftarrow{\Phi}_{\sigma}(z_i^+, t) &= \sum_{t_0=0}^t S_{\sigma}^{\text{eff}}(z_{i+1}, t_0) \psi_{\sigma}(z_i^+, t|z_{i+1}, t_0) + \sum_{\sigma'} [\overleftarrow{T}_{\sigma,\sigma'}(z_{i+1}^+) \overleftarrow{\Phi}_{\sigma'}(z_{i+1}^+, t) + \vec{R}_{\sigma,\sigma'}(z_{i+1}^+) \vec{\Phi}_{\sigma'}(z_{i+1}^+, t)], \end{aligned} \quad (5)$$

where we have introduced the spin-conserving and spin-flipping reflection probabilities for left- and right-moving particles, $\overleftarrow{R}_{\sigma,\sigma'}$ and $\vec{R}_{\sigma,\sigma'}$. Moreover, in Eq. (5) we have introduced the integrated flux, given by ψ_{σ} , for which an analytical expression was given in Ref. [53]. Throughout this paper, we keep the spatial discretization step $\delta z = 1$ nm and time step $\delta t = 1$ fs.

B. Model system

To investigate the influence of noncollinear magnetizations, we model a magnetic multilayer, Al (3 nm)/Ni (5 nm)/Ru (2nm)/Fe (4 nm)/Ru (5 nm), shown schematically in Fig. 1 [26,27]. The magnetic layers, Ni and Fe, are separated by a thin nonmagnetic Ru layer. The magnetization of the Ni magnetic layer is assumed to be aligned with the x axis, while the magnetization of the Fe layer can in general be rotated, in the plane of the layer, by an angle θ from the x axis.

We assume that the laser pulse illuminates the sample from the side of the outer Al layer and that the hot electrons are excited just in the magnetic Ni layer. Moreover, for simplicity, the excited electrons are homogeneously distributed throughout the layer.

A necessary ingredient for solving Eqs. (2)–(5) are the spin- and energy-dependent transmission probabilities through the interfaces between the layers. In the next section (Sec. IIC) we shall describe the method used for calculating these at the material-specific level.

C. The theory of interface scattering

The material-specific transmissions through interfaces or multilayers were obtained using the two-step procedure described in Refs. [45,56]. In the first step the self-consistent

Equation (4) includes the contributions from both the scattered hot electrons, formally treated as newly excited, and the ones actually excited as the result of the scattering. In this way, spin-flip scattering, which is due to spin-orbit interaction, can be included [14] and was studied previously for collinear heterostructures [20]. Here, however, our focus is on spin mixing related to noncollinearity. It is known that spin-orbit coupling can generate spin currents at interfaces as well [54], but considering the spin-flip times calculated for excited electrons in few selected metals [55], we estimate that the effect of spin-orbit coupling on the dominant hot-electron transport in the studied system is small. Therefore we have not taken spin-orbit related spin flips into account.

In order to include multiple transmissions and reflections in Eq. (2) it is beneficial to calculate the total particle fluxes in a recursive way. Following [48,53], the fluxes are obtained from

potentials for a system of interest were calculated using the tight-binding linear muffin-tin orbital (TB-LMTO) method [57,58] in the atomic-sphere approximation (ASA). The potentials were then used to calculate the elements of the scattering matrix, i.e., transmission and reflection coefficients using the wave function matching method [45,56]. The latter step was performed for energies in the interval $[\epsilon_{\text{Fermi}}, \epsilon_{\text{Fermi}} + 1.5 \text{ eV}]$ with a step of 0.125 eV. The length of the interval (1.5 eV) corresponds to the typical energy of the photons from the exciting laser in experiments.

Little is known about the crystalline structure and orientation of the experimental structures [26,27]. We assumed

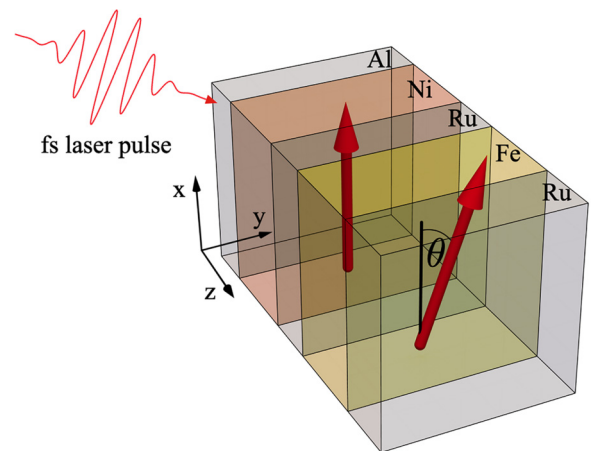


FIG. 1. Model of the studied magnetic multilayer. The laser pulse excites the multilayer on the Al side. The magnetizations of the Ni and Fe layers are noncollinear, expressed by the angle θ between them.

therefore that all the elements grow in their bulk lattice structures, i.e., fcc for Al and Ni, bcc for Fe, and hcp for Ru. Furthermore, we chose the (111) orientation for Al, Ni, and Fe and (0001) for the Ru layer, thus preserving the maximum axial symmetry. The main difficulty arising when performing the calculations is the substantial lattice constant mismatch between the different layers. In order to take this into account we modeled the interfaces using lateral supercells of different sizes. In particular, we used $7 \times 7|8 \times 8$ for the interface between Al ($a_{\text{Al}} = 4.05 \text{ \AA}$) and Ni ($a_{\text{Ni}} = 3.52 \text{ \AA}$), $13 \times 13|12 \times 12$ for Ni and Ru ($a_{\text{Ru}} = 2.71 \text{ \AA}$), and $3 \times 3|2 \times 2$ for Ru and Fe ($a_{\text{Fe}} = 2.87 \text{ \AA}$). The trilayer structure was modeled as Ni(13×13)|Ru(12×12)|Fe(8×8). The adjustments of the in-plane lattice constants, necessary to obtain a perfect match between supercells, were well below 1%. A small tetragonal distortion was additionally introduced in order to keep the volume of the unit cells intact. At the interfaces the distance between the atomic layers was set so as to fulfill the local space-filling requirement of the ASA approximation, with the radii of the atomic spheres kept at their bulk values.

The ASA potentials for the supercell calculations were obtained using a simplified procedure described in Ref. [59]. For each interface, two single unit-cell (1×1) calculations were made with the common lattice constant set first to the value corresponding to the bulk structure of the material to the left and then to the right of the interface. The final interface structure was then constructed using the spheres (and the associated potentials) with the correct radius for either side.

With the transmission and/or reflection coefficients calculated, the energy-dependent Landauer-Büttiker (LB) conductances can be calculated as

$$G(\sigma, \epsilon) = \frac{e^2}{h} \frac{1}{4\pi^2} \int_{2\text{DBZ}} \sum_{\nu\mu} |t_{\nu\mu}^\sigma(k_{\parallel})|^2, \quad (6)$$

where $t_{\nu\mu}^\sigma(k_{\parallel})$ are the scattering coefficients, and the ν and μ are the indices for the modes at opposite sides of the interface, characterized by the same lateral component of the wave vector (k_{\parallel}), and the two-dimensional Brillouin zone (2DBZ) is defined by the matching lateral supercells. In Eq. (6) we implicitly assumed the specular (i.e., k_{\parallel} -preserving) scattering. However, since the interface between non-lattice-matched lattices inherently breaks the lateral translational symmetry, a certain amount of diffusive scattering is still possible even with enforced perfect match between supercells on both sides of the interface. The 2DBZ defined for the $N \times N$ lateral supercell is the folded down version of the original ($N = 1$) zone.¹ Consequently the set of N^2 k_{\parallel} points in the original $N = 1$ zone is now represented by a single point in the folded-down version. All the propagating modes characterized originally by the lateral wave vectors belonging to the N^2 set are now formally treated as having the same k_{\parallel} wave vector. When the supercells on the left and right sides of the interface are matched in external dimensions but differ in multiplicity (i.e., $N_1 a_1 = N_2 a_2$ but $N_1 \neq N_2$, $a_{1(2)}$ being the

left- and right-side lattice constants) the lowering of the symmetry may enable matching between the modes originally (i.e., in unfolded 2DBZs) belonging to different k_{\parallel} wave vectors.

The LB conductance through the interface does not depend on the direction of scattering. The same, however, is not true for the Sharvin conductances

$$\vec{G}_{\text{Sh}}(\sigma, \epsilon) = \frac{e^2}{h} \frac{1}{4\pi^2} \int_{2\text{DBZ}} \sum_{\mu\mu'} \delta_{\mu'\mu} = \frac{e^2}{h} N_L, \quad (7)$$

$$\overleftarrow{G}_{\text{Sh}}(\sigma, \epsilon) = \frac{e^2}{h} \frac{1}{4\pi^2} \int_{2\text{DBZ}} \sum_{\nu'\nu} \delta_{\nu'\nu} = \frac{e^2}{h} N_R, \quad (8)$$

which amount simply to the number of modes (per unit area) in the left (N_L) or right (N_R) lead. Consequently, the averaged transmission for the right- and left-moving electrons,

$$\vec{T}_{\sigma} = \frac{G(\sigma, \epsilon)}{\vec{G}_{\text{Sh}}(\sigma, \epsilon)} \quad \text{and} \quad \overleftarrow{T}_{\sigma} = \frac{G(\sigma, \epsilon)}{\overleftarrow{G}_{\text{Sh}}(\sigma, \epsilon)}, \quad (9)$$

respectively, also assume different values. The transmissions obtained both for single interfaces and for the whole Ni/Ru/Fe trilayer will be discussed in Sec. III.

III. THE TRANSPORT THROUGH INTERFACES

A. Single interfaces

Figure 2 shows the calculated transmissions for hot electrons in the spin-up and spin-down channels as a function of energy for each single interface in the studied multilayer, namely, Al/Ni, Ni/Ru, and Ru/Fe. We show separately the transmissions for electrons moving from the left to the right (top row) and electrons moving from the right to the left (bottom row). In all three cases, one can observe a significant nonlinear dependence of transmission on energy. Moreover, a strong asymmetry between spin-up and spin-down channels is obvious for all three interfaces for some energies.

The results for the Al/Ni interface [Figs. 2(a) and 2(b)] are in agreement with those published recently [48]. The small differences are easily explainable by the different choices of interface geometry, i.e., crystallographic orientations of the respective metals, between Ref. [48] and the present paper.

B. Central nonmagnetic layer

The key part of our model is the treatment of the central nonmagnetic layer, which separates two magnetic layers, Ni and Fe. If the magnetizations in the two magnetic layers are collinear, i.e., parallel or antiparallel, the electronic and spin transport can be described by the two sets of independent equations for the spin-up and spin-down channel, making use of the single-interface transmission parameters shown in Fig. 2. This case has been studied experimentally and modeled using the superdiffusive spin-dependent transport theory in Ref. [26], although without the *ab initio* calculated scattering coefficients.

In the case of a noncollinear magnetic configuration, the spin channels are mixed.² Consequently, the spin currents in the Ru spacer now possess the component perpendicular to

¹Note that the $N = 1$ 2DBZs are generally different for the non-lattice-matched materials. This is the case for our Al/Ni/Ru/Fe multilayer.

²Note that we do not take into account explicit spin-flip scattering at the interfaces.

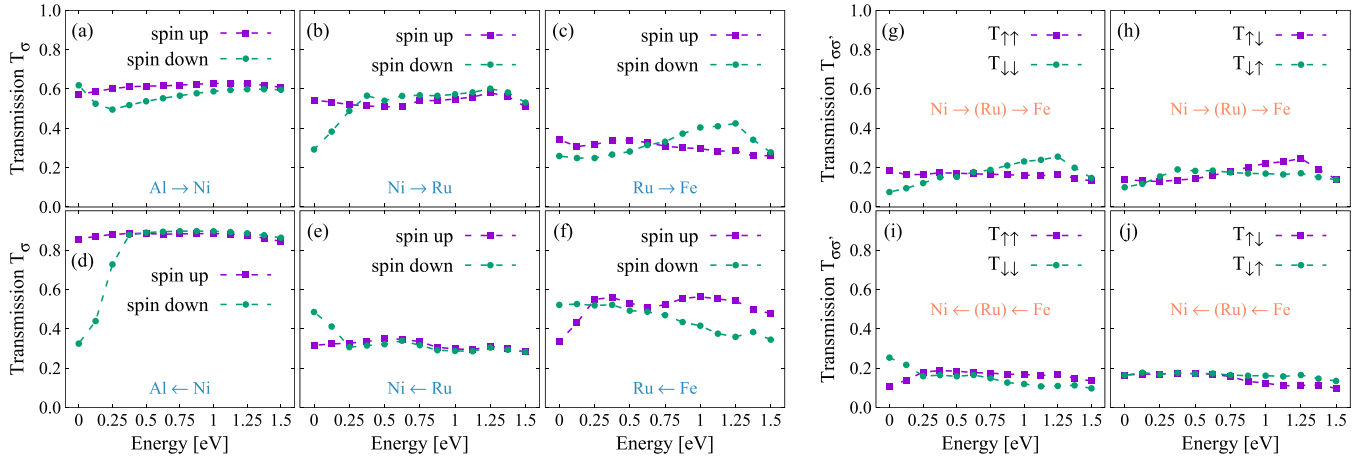


FIG. 2. The spin-dependent transmissions of hot electrons as a function of energy, calculated using *ab initio* methods for each single interface in the Al/Ni/Ru/Fe/Ru multilayer. The top row shows transmissions for electrons moving from the left to the right, while the bottom row shows transmissions for electrons moving from the right to the left.

the magnetizations of magnetic layers. This in turn leads to spin torques acting on the moments of both Ni and Fe layers. In our model, we assume that the central nonmagnetic layer is thin enough ($\sim 1-2$ nm, as in experiment [26]) so that the interface scattering dominates over the contribution from the bulk of the layer.

In order to assess the importance of the multiple internal reflections in the central layer, we shall first consider a simplified model where these are ignored and only the first-order contribution to the total transmission probability is taken into account.

For the electrons moving to the right, we define the diagonal transmission through the single interface as

$$\vec{T}^{(i)} = \begin{pmatrix} \vec{T}_{\uparrow}^{(i)} & 0 \\ 0 & \vec{T}_{\downarrow}^{(i)} \end{pmatrix} \quad (10)$$

with $i = 1, 2$ corresponding to the Ni/Ru and Ru/Fe interfaces, respectively.

Ignoring the internal reflections in the central layer, we can express the total transmission of the spacer and internal interfaces as

$$\vec{T} = \vec{T}^{(1)} \underline{\mathcal{R}}(\theta) \vec{T}^{(2)}, \quad (11)$$

where $\underline{\mathcal{R}}(\theta)$ is the spin rotation matrix due to noncollinear magnetic configurations of Ni and Fe, defined as

$$\underline{\mathcal{R}}(\theta) = \begin{pmatrix} \cos^2(\theta/2) & \sin^2(\theta/2) \\ \sin^2(\theta/2) & \cos^2(\theta/2) \end{pmatrix}, \quad (12)$$

with θ being the angle between their magnetizations. The transmissions introduced in Eqs. (9) and (10) are *probabilities*, therefore the formula for total transmission explicitly assumes the loss of coherence between the two interfaces.

Finally, we obtain

$$\vec{T} = \begin{pmatrix} \vec{T}_{\uparrow\uparrow} \cos^2(\theta/2) & \vec{T}_{\uparrow\downarrow} \sin^2(\theta/2) \\ \vec{T}_{\downarrow\uparrow} \sin^2(\theta/2) & \vec{T}_{\downarrow\downarrow} \cos^2(\theta/2) \end{pmatrix}, \quad (13)$$

where

$$\vec{T}_{\uparrow\uparrow} = \vec{T}_{\uparrow}^{(1)} \vec{T}_{\uparrow}^{(2)}, \quad (14a)$$

$$\vec{T}_{\uparrow\downarrow} = \vec{T}_{\uparrow}^{(1)} \vec{T}_{\downarrow}^{(2)}, \quad (14b)$$

$$\vec{T}_{\downarrow\uparrow} = \vec{T}_{\downarrow}^{(1)} \vec{T}_{\uparrow}^{(2)}, \quad (14c)$$

$$\vec{T}_{\downarrow\downarrow} = \vec{T}_{\downarrow}^{(1)} \vec{T}_{\downarrow}^{(2)}. \quad (14d)$$

Assuming electrons moving from the left to the right, we can express the currents in the right magnetic layer as

$$\begin{pmatrix} \vec{J}_{\uparrow}^R \\ \vec{J}_{\downarrow}^R \end{pmatrix} = \vec{T} \begin{pmatrix} \vec{J}_{\uparrow}^L \\ \vec{J}_{\downarrow}^L \end{pmatrix}, \quad (15)$$

where \vec{J}_{σ}^L and \vec{J}_{σ}^R are the majority and minority spin-channel currents in the left and right magnetic layer, respectively. Note that the σ in the present context should be read as relative to the local magnetization, i.e., it denotes the local majority or minority character rather than the global orientation of electron spin.

Working out Eq. (15) we can write

$$\vec{J}_{\uparrow}^R = \vec{T}_{\uparrow\uparrow} \cos^2(\theta/2) \vec{J}_{\uparrow}^L + \vec{T}_{\uparrow\downarrow} \sin^2(\theta/2) \vec{J}_{\downarrow}^L, \quad (16a)$$

$$\vec{J}_{\downarrow}^R = \vec{T}_{\downarrow\uparrow} \sin^2(\theta/2) \vec{J}_{\uparrow}^L + \vec{T}_{\downarrow\downarrow} \cos^2(\theta/2) \vec{J}_{\downarrow}^L. \quad (16b)$$

The spin reflections and transmissions have to obey

$$\vec{R}_{\uparrow} + \vec{T}_{\uparrow\uparrow} \cos^2(\theta/2) + \vec{T}_{\downarrow\uparrow} \sin^2(\theta/2) = 1, \quad (17a)$$

$$\vec{R}_{\downarrow} + \vec{T}_{\downarrow\downarrow} \cos^2(\theta/2) + \vec{T}_{\uparrow\downarrow} \sin^2(\theta/2) = 1, \quad (17b)$$

where \vec{R}_{\uparrow} and \vec{R}_{\downarrow} are reflections for electrons without a change of their spin. Spin-flip reflections from the interfaces are not taken into account. Thus, the reflected currents on the left-hand side (moving to the left) read

$$\vec{J}_{\uparrow}^L = [1 - T_{\uparrow\uparrow} \cos^2(\theta/2) - T_{\downarrow\uparrow} \sin^2(\theta/2)] \vec{J}_{\uparrow}^L, \quad (18a)$$

$$\vec{J}_{\downarrow}^L = [1 - T_{\downarrow\downarrow} \cos^2(\theta/2) - T_{\uparrow\downarrow} \sin^2(\theta/2)] \vec{J}_{\downarrow}^L. \quad (18b)$$

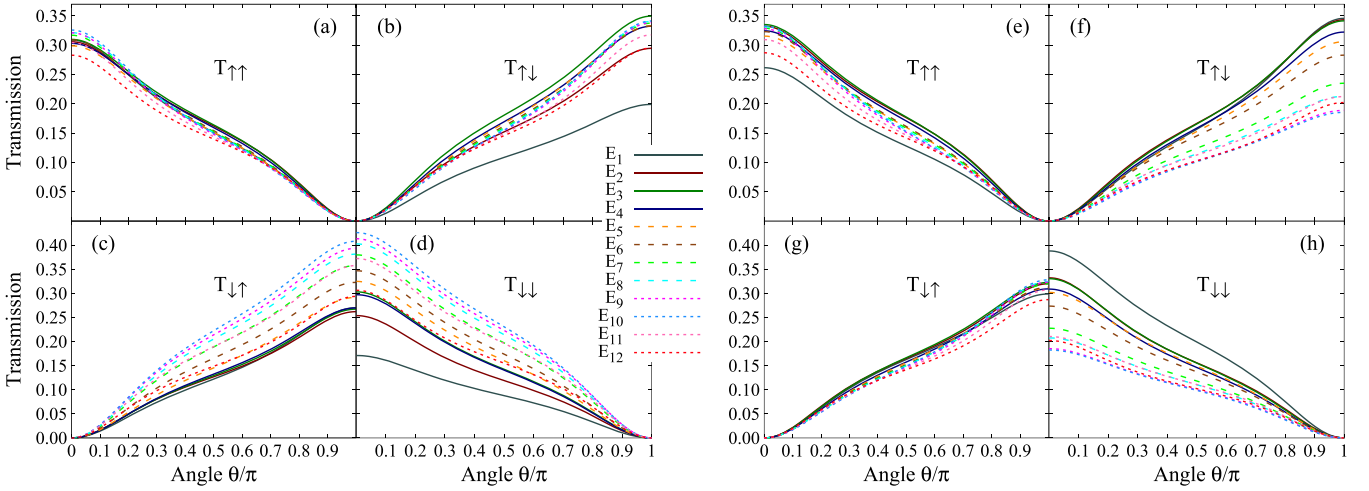


FIG. 3. Angular dependence of the total transmission through the nonmagnetic spacer assuming multiple scattering in the central Ru layer calculated for 12 energy levels above the Fermi energy, $E_n = (0.125 \text{ eV})n$. Panels (a)–(d) show transmissions for electrons moving from the left to the right, while panels (e)–(h) correspond to transmissions of electrons moving from the right to the left. The diagonal elements $T_{\uparrow\uparrow}$, shown in (a) and (e), and $T_{\downarrow\downarrow}$, shown in (d) and (h), describe spin-conserving transmissions for the spin-up and the spin-down channel, respectively. The off-diagonal elements, $T_{\uparrow\downarrow}$, shown in (b) and (f), and $T_{\downarrow\uparrow}$, shown in (c) and (g), denote the spin-flip transmissions of electrons changing their spin from down to up and up to down, respectively.

Analogically, by interchanging the electrons' directions, one can rewrite Eqs. (10)–(18) for the currents moving in the opposite direction.

C. Multiple scattering

The full treatment of the hot electron transiting through the Ni/Ru/Fe trilayer requires taking into account the multiple internal reflections within the Ru spacer. The total transmission matrix for electrons moving from the left to the right is defined as

$$\vec{T} = \vec{T}^{(2)} \mathcal{R}(\theta) \left[\sum_{n=0}^{\infty} (\overleftarrow{R}^{(1)} \mathcal{R}(\theta) \overrightarrow{R}^{(2)} \mathcal{R}(\theta))^n \right] \vec{T}^{(1)}, \quad (19)$$

where

$$\overleftarrow{R}^{(1)} = \underline{I} - \overleftarrow{T}^{(1)} = \begin{pmatrix} \overleftarrow{R}_{\uparrow}^{(1)} & 0 \\ 0 & \overleftarrow{R}_{\downarrow}^{(1)} \end{pmatrix} \quad (20)$$

is the reflection matrix of the first interface (Ni/Ru) for electrons moving to the left, where \underline{I} is the 2×2 unit matrix, and

$$\overrightarrow{R}^{(2)} = \underline{I} - \overrightarrow{T}^{(2)} = \begin{pmatrix} \overrightarrow{R}_{\uparrow}^{(2)} & 0 \\ 0 & \overrightarrow{R}_{\downarrow}^{(2)} \end{pmatrix} \quad (21)$$

is the reflection matrix of the second interface (Ru/Fe) for electrons moving to the right. It can be easily seen that the simplified transmission given by Eq. (11) is the first term of the series which constitutes the full transmission in Eq. (19). Even though formula (19) now incorporates the possibility of multiple internal reflections, it still assumes, just like the simplified version, the lack of coherence.

Similarly, we can define the total transmission matrix for electrons moving from the right to the left as

$$\overleftarrow{T} = \overleftarrow{T}^{(1)} \mathcal{R}(\theta) \left[\sum_{n=0}^{\infty} (\overrightarrow{R}^{(2)} \mathcal{R}(\theta) \overleftarrow{R}^{(1)} \mathcal{R}(\theta))^n \right] \overleftarrow{T}^{(2)}. \quad (22)$$

In the parallel magnetic configuration, for $\theta = 0$, the above equations lead to

$$\overrightarrow{T}_{\sigma} = \overrightarrow{T}_{\sigma}^{(1)} \overrightarrow{T}_{\sigma}^{(2)} \left[\sum_{n=0}^{\infty} (\overleftarrow{R}_{\sigma}^{(1)} \overrightarrow{R}_{\sigma}^{(2)})^n \right], \quad (23a)$$

$$\overleftarrow{T}_{\sigma} = \overleftarrow{T}_{\sigma}^{(1)} \overleftarrow{T}_{\sigma}^{(2)} \left[\sum_{n=0}^{\infty} (\overleftarrow{R}_{\sigma}^{(1)} \overrightarrow{R}_{\sigma}^{(2)})^n \right], \quad (23b)$$

for both $\sigma \in \{\uparrow, \downarrow\}$, which have as solutions

$$\overrightarrow{T}_{\sigma} = \frac{\overrightarrow{T}_{\sigma}^{(1)} \overrightarrow{T}_{\sigma}^{(2)}}{1 - \overleftarrow{R}_{\sigma}^{(1)} \overrightarrow{R}_{\sigma}^{(2)}}, \quad (24a)$$

$$\overleftarrow{T}_{\sigma} = \frac{\overleftarrow{T}_{\sigma}^{(1)} \overleftarrow{T}_{\sigma}^{(2)}}{1 - \overleftarrow{R}_{\sigma}^{(1)} \overrightarrow{R}_{\sigma}^{(2)}}. \quad (24b)$$

Thus, considering internal multiple reflections in the nonmagnetic spacer might substantially increase the total transmissions. Moreover, the angular dependence of the transmissions might depart from the simple sinelike dependence. Figure 3 shows the angular dependence of the transmission probabilities calculated for different energies, $E_n = (0.125 \text{ eV})n$ with $n = 1, 2, \dots, 12$, above the Fermi level.

Figures 3(a)–3(d) show transmissions for electrons moving from the left to the right, while Figs. 3(e)–3(h) contain transmissions for electrons moving from the right to the left. In both cases we show the diagonal elements of the transmission matrices, $T_{\uparrow\uparrow}$ and $T_{\downarrow\downarrow}$, which correspond to spin-conserving transmissions through the spacer for the spin-up and the spin-down channel, respectively. The off-diagonal elements of the

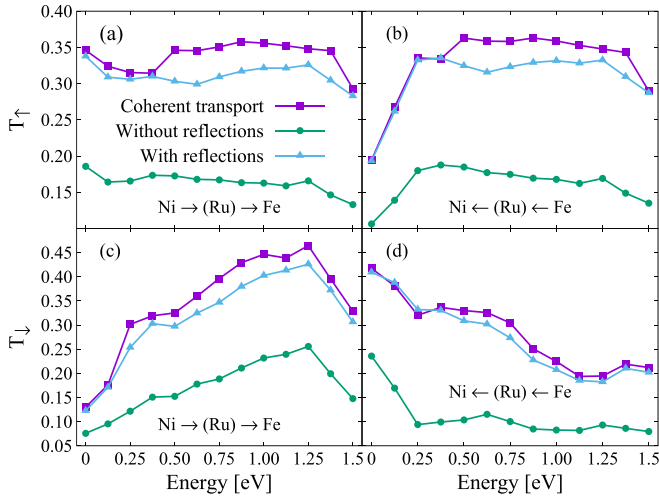


FIG. 4. Comparison of the energy dependence of electron transmissions through the nonmagnetic spacer of Ni/Ru/Fe, calculated using three different models: quantum coherent transport (squares), Eq. (11) without considering multiple internal reflections in the Ru layer (circles), and Eq. (19) considering internal multiple reflections of electrons on the Ru interfaces (triangles). Panels (a) and (b) show transmissions of electrons in the spin-up channel, while panels (c) and (d) show transmissions of electrons in the spin-down channel. In panels (a) and (c) we plot transmissions of electrons moving from the left to the right (Ni \rightarrow Fe); in panels (b) and (d) transmissions for electrons moving from the right to the left (Ni \leftarrow Fe) are plotted.

transmission matrix, $T_{\uparrow\downarrow}$ and $T_{\downarrow\uparrow}$, correspond to the spin-flip transmissions, which mix the spin channels. Obviously, the spin-conserving transmissions reach their maximum for $\theta = 0$, i.e., in the parallel magnetic configuration, when the spin-flip terms reach zero. Oppositely, for $\theta = \pi$, i.e., in the antiparallel magnetic configuration, the electrons passing the nonmagnetic spacer are injected into the opposite spin channel. Thus, the spin-flip transmissions are maximal, while the spin-conserving transmissions disappear.

The above described model for the transmissions of electrons through the noncollinear system combines the results of *ab initio* calculations with the classical formula for noncoherent multiple reflections. To test the model we shall compare the transmissions obtained from (11) and (19) with the results of explicit calculations, by using the method outlined in Sec. II C, of spin-dependent transmission through the Ni/Ru (2 nm)/Fe trilayer, where Ni and Fe form the semi-infinite electrodes.

A comparison of all three models of the Ni/Ru/Fe transmissions is shown in Fig. 4. Comparing the semiclassical transport model with and without internal reflections, one can notice a significant increase of transmissions when reflections are included. Furthermore, it can be seen that the semiclassical approach including internal multiple reflections is in reasonably good agreement with the fully quantum-mechanical approach. Therefore, in the next sections we shall adapt the semiclassical approach including multiple internal reflections to model the spin-dependent transport through the thin nonmagnetic spacer.

Having established the way to calculate transmissions for a noncollinear system, we can now proceed with the solution of Eq. (2). From this equation we obtain the time dependence of the spin density as well as spin fluxes for each energy and spin channel in each point of the discretized trilayer. This allows us to inspect the laser-induced demagnetization in the magnetic layers and to define the spin-transfer torques acting on the magnetizations. The results will be discussed in the following sections.

IV. DEMAGNETIZATION

In this section we focus on the effect of laser-induced ultrafast demagnetization in the studied trilayer. We start with the collinear magnetic configurations. Since this case can be described within the original model of superdiffusive hot-electrons transport [53], the comparison of the results with the model used in this paper will serve as a test of the validity of our approach, in particular the assumption of the negligible spacer thickness. In the latter part of this section, we will focus on the angular dependence of the demagnetization in both magnetic layers.

In our calculations we assumed that the original nonthermal excitation is caused by the Gaussian laser pulse with the halfwidth $t_p = 35$ fs. In the experimental study by Rudolf *et al.*, Al and Ni layers together absorb more than 58% of the incident light, which was about 2.5 times as much as the Fe layer [26]. Thus, for simplicity, we assumed that the excited electrons are homogeneously distributed throughout the Ni layer and nowhere else. The energy distribution of the excited population was set to be constant over the interval $[\epsilon_{\text{Fermi}}, \epsilon_{\text{Fermi}} + 1.5 \text{ eV}]$. In the calculations the energy dependence over this range was discretized on a grid with $\Delta\epsilon = 0.125 \text{ eV}$, known from previous experience to be sufficiently precise. We assumed that the areal electron density excited by the laser pulse is 0.1 electron per energy/spin level in each computational cell of the Ni layer. This value roughly corresponds to an energy density absorbed in the 5 nm Ni layer of $\sim 4.7 \text{ mJ/cm}^2$ (cf. [60]). Since the numbers of excited electrons scale linearly with the excitation density, they can be simply recalculated for any laser intensity.

A. Collinear magnetic configurations

Figure 5 shows the time evolution of the magnetization in the Ni and Fe magnetic layer in the studied multilayer due to the laser pulse, calculated for the collinear magnetic configurations, parallel (P) and antiparallel (AP). The results for varying thickness of the Ru spacer, given by x , are plotted using the lines of different type and color. The $x = 0.0 \text{ nm}$ case was calculated using the multiple-reflections formulas (19) and (22) and the values of interface transmissions from Figs. 2(a)–2(f). The finite thickness cases were calculated using the standard, collinear version of the superdiffusive transport model of Ref. [53] which is applicable in this case. Note that the multiple reflections within the spacer are naturally included in this version of the formalism. We further note that (diffusive) remagnetization processes [61] are not included in the simulations.

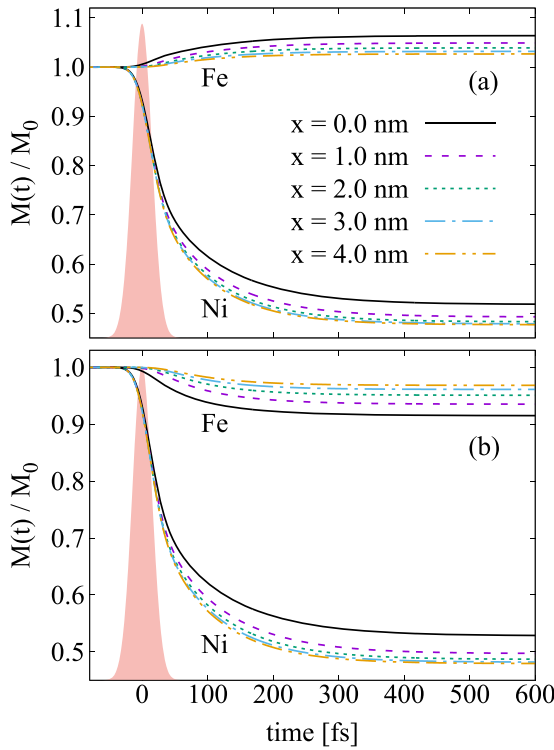


FIG. 5. Time dependence of the magnetization of the Fe and Ni layer in the Al(3)/Ni(5)/Ru(x)/Fe(5)/Ru multilayer due to the laser pulse, (a) in the parallel magnetic configuration, and (b) in the antiparallel magnetic configuration. The time dependence of the laser fluence is given by the red filled area.

Comparing the results for $x = 0$ with the finite-width spacer model, one can see a qualitative agreement of both models. Importantly, in accord with the previous calculations and experiments [26] we observe an *enhancement* of the Fe magnetization in the P configuration. In the AP configuration the magnetizations decrease in both layers. As the spacer width increases, the demagnetization of the Ni layer increases. This is because in the model with $x = 0$, electrons moving towards the Fe layer have to overcome the total reflectivity of both interfaces (Ni/Ru and Ru/Fe). In the model with finite thickness the electrons can flow into the Ru layer. Since the transmission of Ni/Ru interface [Fig. 2(b)] is much higher than that of the effective Ni/Fe interface [Fig. 2(g)], the demagnetization is higher when $x > 0$. Moreover, with increasing x , the demagnetization approaches a constant value, which is a sign of a finite spin diffusion length in the Ru layer. Similarly, in the P configuration the laser-induced magnetization enhancement in the Fe layer becomes smaller as x increases, because some electrons relax in the Ru layer, or are reflected from the Ru/Fe interface. Oppositely, in the AP configuration one can observe a smaller demagnetization in the Fe layer for the same reason.

We can conclude that the zero-width model does reproduce correctly the trends observed in calculations with a finite spacer thickness. What's more, the numerical results do not deviate too strongly from those corresponding to experimental thicknesses, i.e., $x \sim 1\text{--}2$ nm.

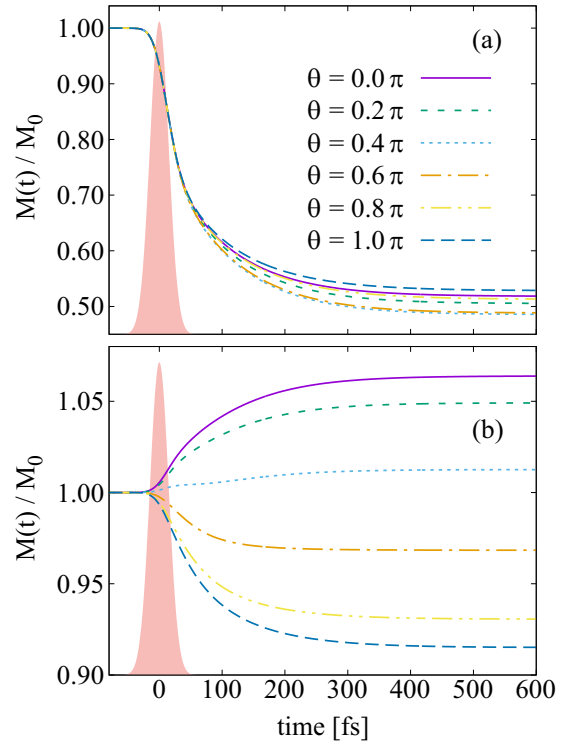


FIG. 6. Time dependence of the magnetization in (a) the nickel and (b) the iron layer caused by the femtosecond laser pulse, calculated in the collinear and noncollinear magnetic configurations given by the angle θ . The time dependence of the laser fluence is given by the red filled area.

B. Noncollinear magnetic configurations

Next we shall focus on the noncollinear magnetic configurations. Figure 6 shows the demagnetization of Ni and Fe layers calculated for different angles between their magnetization directions. The calculations were done in the zero-width spacer limit. First, we can notice that the magnetic configuration of the Fe layer, given by angle θ , has almost no influence on the demagnetization of the Ni layer. This is because Ni is demagnetized directly by the laser pulse. The electrons reflected from the spacer or secondary electrons generated in the multilayer have just a minor effect on the total demagnetization of Ni. In contrast, the magnetization of the Fe layer is strongly affected by the magnetic configuration. As the angle θ changes from 0 to π , we can see a direct crossover from magnetization enhancement in the Fe layer, to magnetization reduction. In Fig. 7 we plot the total angular dependence of the demagnetization as a function of θ . To this end, we calculated the magnetization of the Ni and Fe layers after 2 ps, when all the spin currents in the system have become zero. While the Fe magnetization monotonously decreases with θ , the magnetization in the Ni layer shows a global minimum, which, although shallow, corresponds to a maximum demagnetization for a certain noncollinear configuration as shown in Fig. 7.

V. SPIN-TRANSFER TORQUE

Lastly, we inspect the spin-transfer torque acting on both magnetic layers. To define the STT action in the Fe magnetic

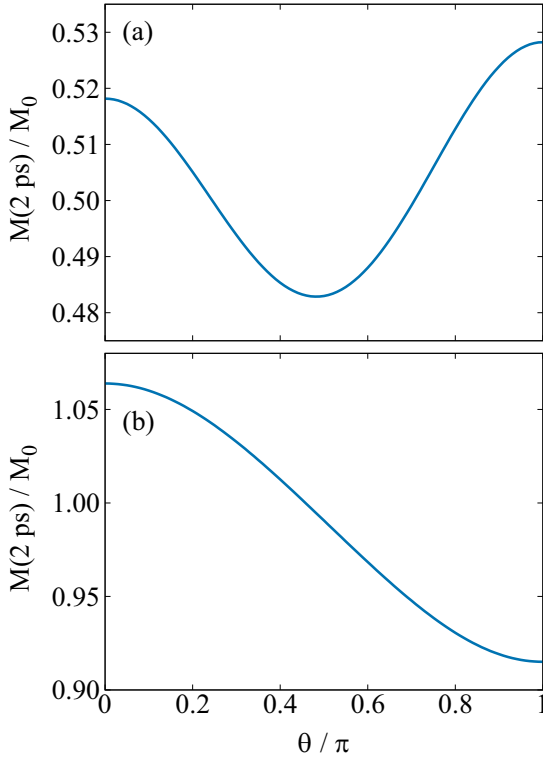


FIG. 7. The magnetization of (a) the nickel layer and (b) the iron layer as a function of angle θ between the magnetizations, calculated at 2 ps after irradiation with a femtosecond laser pulse.

layer, we need to calculate the spin current of the electrons moving from the left to the right at the left- and right-hand sides of the Ru spacer. In other words, we need to calculate the spin current heading from Ni to the Ru spacer and the one incoming into the Fe layer. The spin current is calculated as [62]

$$\vec{J}_s(t) = \frac{\hbar}{2} \sum_{i=1}^{N_\epsilon} [\vec{j}'_{\uparrow}(\epsilon_i, t) - \vec{j}'_{\downarrow}(\epsilon_i, t)] \hat{m}_{\text{Ni}}, \quad (25)$$

where $N_\epsilon = 12$ is the number of the hot electrons energy levels used in the simulation, and \hat{m}_{Ni} is a unit vector along the Ni magnetization. Likewise, the spin current on the right-hand side is given by

$$\vec{J}'_s(t) = \frac{\hbar}{2} \sum_{i=1}^{N_\epsilon} [\vec{j}'_{\uparrow}(\epsilon_i, t) - \vec{j}'_{\downarrow}(\epsilon_i, t)] \hat{m}_{\text{Fe}}, \quad (26)$$

where \hat{m}_{Fe} is a unit vector along the Fe magnetization. Note that the form of Eqs. (25) and (26) describes only the longitudinal spin currents with implicit assumption that the transversal components are entirely absorbed in the interface zone (cf. [63]). The total spin-transfer torque acting on the Fe magnetization is thus [64]

$$\tau_{\text{Fe}} = -[\mathbf{J}_s(t) - \mathbf{J}'_s(t)]. \quad (27)$$

The STT τ_{Fe} cannot influence the magnitude of the magnetization. Thus, we are interested only in the STT component, which lies in the plane defined by the vectors \hat{m}_{Ni} and \hat{m}_{Fe} ,

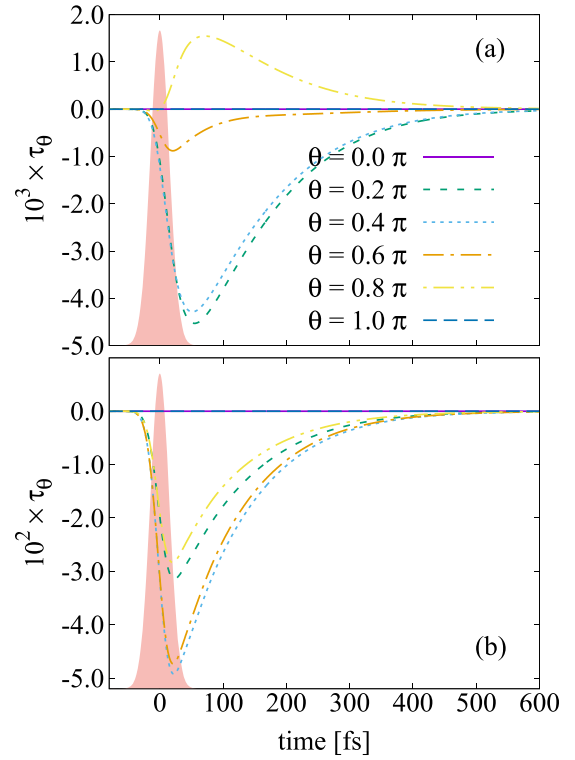


FIG. 8. Time dependence of the spin-transfer torque acting on (a) the Ni and (b) the Fe magnetization, excited by a femtosecond laser pulse per area of a^2 with a being the crystal lattice constant. The STT is calculated for different magnetic configurations given by the angle between the magnetizations, θ . The STT is given in units of $(\hbar/2)$ fs $^{-1}$. The red filled area corresponds to the time dependence of the laser pulse.

which can change the angles between the two magnetizations,

$$\tau_{\theta \text{ Fe}}(t) = \tau_{\text{Fe}} \cdot \hat{e}_\theta, \quad (28)$$

where $\hat{e}_\theta = (\cos \theta, 0, -\sin \theta)$. Analogously, one can define the STT acting on the Ni magnetic layer, taking into account hot electrons moving from the Fe magnetic layer through the Ru spacer. Figure 8 depicts the time dependence of the spin-transfer torque action in the magnetic layers at different magnetic configurations given by the mutual angle, θ . As expected, there is no spin-transfer torque in the collinear magnetic configurations. Let us start with the analysis of the STT action on the Fe magnetizations, shown in Fig. 8(b). Both its onset and maximum correlate closely with the same features of the laser pulse itself, with the delay being practically nonexistent for the onset and only about 20 fs for the maximum. This suggests that the torque acting in the Fe layer is primarily generated by the hot electrons, which were excited directly by the laser pulse in the Ni layer. Afterwards it starts to decrease, which is a consequence of hot electrons' relaxation and decay of the spin currents. The spin-transfer torque in the Fe layer disappears after ~ 300 fs. Moreover, we can see that the torque in the Fe layer appears to be roughly symmetric with respect to $\theta = \pi/2$.

Let us focus now on the action of the torque on the moment of the Ni layer, shown in Fig. 8(a). The STT acting in this layer is mostly generated by the left-moving electrons coming

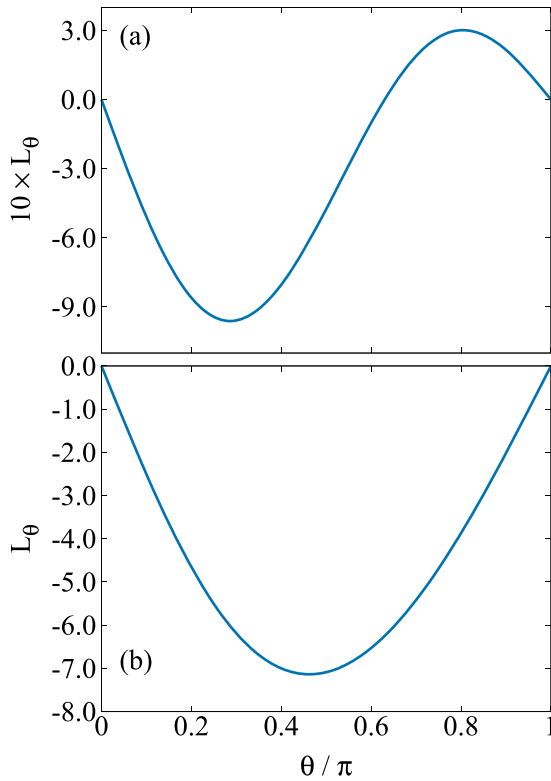


FIG. 9. Angular dependence of the total angular momentum due to hot electron-induced STT absorbed in (a) the Ni, and (b) the Fe magnetic layer per area of a^2 with a being the crystal lattice constant. L_θ is given in the units of $\hbar/2$.

from the direction of the Fe layer. These are the hot electrons reflected from the interfaces or the secondary ones excited in the Fe layer. Therefore, the STT magnitude in the Ni layer is about ten times smaller than that in Fe. One can also notice a later onset and longer time required for reaching the maximum value of the STT than in the Fe layer. The origin of the electrons that generate a torque in Ni is recognized in its angular dependence, too. In contrast to the STT in Fe, the torque in the Ni layer shows a significant asymmetry with respect to $\theta = \pi/2$. More importantly, when the angle θ becomes closer to the AP magnetic configuration, the STT changes its direction (sign) after some time, which can be seen for curves calculated for $\theta = 0.8\pi$.

As we can see from Fig. 8, the variation of the STT due to laser-induced hot-electron transport is by far faster than the expected magnetization response, which is usually in the gigahertz regime. Therefore, we argue that the total layer magnetization will respond to the total momentum absorbed in the layer rather than the time-dependent STT. Therefore, in Fig. 9 we show the angular dependence of the total momentum absorbed in the magnetic layer defined as

$$L_\theta(\theta) = \int_{-\infty}^{\infty} dt \tau_\theta(\theta, t). \quad (29)$$

As expected, L_θ in the Fe layer is a sinelike function with its maximum close to $\theta = \pi/2$. On the other hand, L_θ in the Ni layer, which is about ten times smaller than that in the Fe

layer, shows a strongly asymmetric behavior and changes its sign in certain noncollinear magnetic configurations.

VI. DISCUSSION AND CONCLUSIONS

We presented results of our analysis of laser-induced transport in magnetic multilayers consisting of Al/Ni/Ru/Fe/Ru layers. The effect of the interfaces was included in the superdiffusive transport model via the spin- and energy-dependent averaged reflection and transmission probabilities. These were calculated, for all interfaces separately at first, using the combination of the *ab initio* TB-LMTO and WFM [44,45] methods. The central part of the multilayer, Ni/Ru/Fe, was treated as a single, effective interface. In this case the parameters were obtained using a semiclassical formula for adding transmissions through two single interfaces. To test the validity of the semiclassical approximation we have compared the results for collinear magnetic configuration with those obtained directly from the TB-LMTO/WFM method. We have found that the results of the fully quantum-mechanical calculations can be successfully approximated using the semiclassical formula, as long as multiple internal reflections are taken into account.

In order to treat noncollinear magnetic configurations, we have extended the standard model of superdiffusive spin-dependent transport [53]. We approximated the central, thin nonmagnetic Ru spacer, separating two magnetic layers, Ni and Fe, as a single, effective interface with its transport properties parametrized by the reflection and transmission probabilities. The averaged scattering probabilities were calculated in a way allowing for including both the impact of multiple (noncoherent) scattering at internal interfaces and the mixing of the spin channels present for the noncollinear configurations.

The accuracy of our treatment of the central nonmagnetic layer has been tested in collinear magnetic configurations by comparing the demagnetization in the magnetic layers calculated in the current approximation (with zero spacer thickness) to that calculated using a model with finite spacer thickness [53]. There is a qualitative agreement between both models; however, quantitatively we observe differences. Our approach provides a slightly smaller demagnetization of the Ni layer. On the other hand, one observes a stronger effect in the Fe magnetic layer. These effects can be explained by the omission of the bulk part of the Ru layer in our model. More specifically, in the nonzero-thickness-spacer model, the effect in the Fe layer is reduced due to electron scattering in the Ru spacer during the superdiffusive transport. This effect is not included in the transport parameters in the current model with zero-thickness Ru spacer.

Our calculations reproduced the main features of ultrafast demagnetization observed in experiment [26], i.e., ultrafast demagnetization of the Ni and Fe layer in the parallel magnetic configuration, and ultrafast increase of the magnetization in the Fe layer in the antiparallel one. In addition to this, we have shown that there is a smooth transition between negative and positive change of magnetization in the Fe layer as the angle between Ni and Fe magnetization vectors varies from 0 to π . On the other hand, for the studied multilayer, the demagnetization of the Ni magnetic layer does not seem to

be meaningfully affected by the magnetic configuration. Consequently, for a certain noncollinear magnetic configuration, one can observe demagnetization in the Ni magnetic layer, but effectively no total change of magnetization in the Fe layer.

We also studied the spin-transfer torque acting in both magnetic layers. When hot electrons were excited just in Ni, the spin current flows mainly from Ni towards the Fe layer and leads to a spin-transfer torque acting on the Fe magnetization. Our simulations have shown that the total transverse angular momentum (time-integrated spin-transfer torque) passing the nonmagnetic spacer depends on the angle between magnetizations as a sinelike function, which resembles the regular (“cold”) spin-transfer torque in magnetic spin valves [1,64]. We also observed a spin current flowing from Fe towards the Ni layer. This spin current consists of electrons reflected from the Ru/Fe interface and also of hot electrons excited secondarily in the Fe layer. Interestingly, the STT changes sign when the angle between the magnetization of Fe and Ni layers exceeds $\theta \approx 0.6\pi$. The reason for this behavior is that for these values of θ the reflected electrons become polarized mostly in the direction of the Fe magnetization. Consequently, the angular dependence of the total transverse angular momentum passing from Fe to the Ni layer becomes zero at certain noncollinear configurations and then changes its sign for increased angles.

In summary, the model presented in this paper fills the gap in the current research of the laser-induced spin transport in multilayered nanostructures. On the one hand, we provided a systematic study of the effect of a thin nonmagnetic

spacer, including its interfaces, on the laser-pulse-induced demagnetization in the magnetic layers. The proper treatment of the interfaces might have a crucial role in explanation of the contrasting results of some recent experimental studies [26,27]. On the other hand, our study goes beyond the standard examination of laser-induced transport in the collinear magnetic configurations, and allows one to study nonequilibrium electronic spin transport in noncollinear magnetic heterostructures, which might open new ways toward laser-driven magnetization switching in spintronic devices.

ACKNOWLEDGMENTS

This work was supported by the Ministry of Education, Youth and Sports of the Czech Republic through the e-INFRA CZ (ID:90140), by the Czech Science Foundation (Grant No. 19-13659S), by the Swedish Research Council (VR), the Knut and Alice Wallenberg Foundation (Grant No. 2022.0079), and by The Ministry of Education, Youth and Sports from the Large Infrastructures for Research, Experimental Development and Innovations project “e-Infrastructure CZ–LM2018140.” This work has furthermore been funded by the European Union’s Horizon2020 Research and Innovation Programme under FET-OPEN Grant Agreement No. 863155 (s-Nebula). We acknowledge computational resources provided by the Swedish National Infrastructure for Computing (SNIC), partially funded by the Swedish Research Council through Grant Agreement No. 2018-05973.

- [1] J. Slonczewski, *J. Magn. Magn. Mater.* **159**, L1 (1996).
- [2] L. Berger, *Phys. Rev. B* **54**, 9353 (1996).
- [3] I. M. Miron, K. Garello, G. Gaudin, P.-J. Zermatten, M. V. Costache, S. Auffret, S. Bandiera, B. Rodmacq, A. Schuhl, and P. Gambardella, *Nature (London)* **476**, 189 (2011).
- [4] L. Liu, C.-F. Pai, Y. Li, H. W. Tseng, D. C. Ralph, and R. A. Buhrman, *Science* **336**, 555 (2012).
- [5] K. Jhuria, J. Hohlfeld, A. Pattabi, E. Martin, A. Y. A. Córdova, X. Shi, R. L. Conte, S. Petit-Watlot, J. C. Rojas-Sanchez, G. Malinowski, S. Mangin, A. Lemaître, M. Hehn, J. Bokor, R. B. Wilson, and J. Gorchon, *Nat. Electron.* **3**, 680 (2020).
- [6] J. E. Hirsch, *Phys. Rev. Lett.* **83**, 1834 (1999).
- [7] J. Sinova, S. O. Valenzuela, J. Wunderlich, C. H. Back, and T. Jungwirth, *Rev. Mod. Phys.* **87**, 1213 (2015).
- [8] E. Beaurepaire, J.-C. Merle, A. Daunois, and J.-Y. Bigot, *Phys. Rev. Lett.* **76**, 4250 (1996).
- [9] K. Carva, P. Baláž, and I. Radu, in *Handbook of Magnetic Materials*, edited by E. Brück (Elsevier, New York, 2017), Vol. 26, pp. 291–463.
- [10] P. Němec, E. Rozkotová, N. Tesarová, F. Trojánek, E. De Ranieri, K. Olejník, J. Zemen, V. Novák, M. Cukr, P. Malý, and T. Jungwirth, *Nat. Phys.* **8**, 411 (2012).
- [11] N. Tesarová, P. Němec, E. Rozkotová, J. Zemen, T. Janda, D. Butkovičová, F. Trojánek, K. Olejník, V. Novák, P. Malý, and T. Jungwirth, *Nat. Photonics* **7**, 492 (2013).
- [12] G. Malinowski, F. Dalla Longa, J. H. H. Rietjens, P. V. Paluskar, R. Huijink, H. J. M. Swagten, and B. Koopmans, *Nat. Phys.* **4**, 855 (2008).
- [13] M. Battiato, K. Carva, and P. M. Oppeneer, *Phys. Rev. Lett.* **105**, 027203 (2010).
- [14] M. Battiato, K. Carva, and P. M. Oppeneer, *Phys. Rev. B* **86**, 024404 (2012).
- [15] A. Melnikov, I. Razdolski, T. O. Wehling, E. T. Papaioannou, V. Roddatis, P. Fumagalli, O. Aktsipetrov, A. I. Lichtenstein, and U. Bovensiepen, *Phys. Rev. Lett.* **107**, 076601 (2011).
- [16] E. Turgut, C. La-o-vorakiat, J. M. Shaw, P. Grychtol, H. T. Nembach, D. Rudolf, R. Adam, M. Aeschlimann, C. M. Schneider, T. J. Silva, M. M. Murnane, H. C. Kapteyn, and S. Mathias, *Phys. Rev. Lett.* **110**, 197201 (2013).
- [17] A. J. Schellekens, K. C. Kuiper, R. R. J. C. de Wit, and B. Koopmans, *Nat. Commun.* **5**, 4333 (2014).
- [18] G.-M. Choi, B.-C. Min, K.-J. Lee, and D. G. Cahill, *Nat. Commun.* **5**, 4334 (2014).
- [19] N. Bergeard, M. Hehn, S. Mangin, G. Lengaigne, F. Montaigne, M. L. M. Laliou, B. Koopmans, and G. Malinowski, *Phys. Rev. Lett.* **117**, 147203 (2016).
- [20] M. Hofherr, P. Maldonado, O. Schmitt, M. Berritta, U. Bierbrauer, S. Sadashivaiah, A. J. Schellekens, B. Koopmans, D. Steil, M. Cinchetti, B. Stadtmüller, P. M. Oppeneer, S. Mathias, and M. Aeschlimann, *Phys. Rev. B* **96**, 100403(R) (2017).
- [21] G. Malinowski, N. Bergeard, M. Hehn, and S. Mangin, *Eur. Phys. J. B* **91**, 98 (2018).
- [22] I. Kumberg, E. Golias, N. Pontius, R. Hosseinifar, K. Frischmuth, I. Gelen, T. Shinwari, S. Thakur, C. Schüßler-Langeheine, P. M. Oppeneer, and W. Kuch, *Phys. Rev. B* **102**, 214418 (2020).

- [23] F. Kühne, Y. Beyazit, B. Sothmann, J. Jayabalan, D. Diesing, P. Zhou, and U. Bovensiepen, *Phys. Rev. Res.* **4**, 033239 (2022).
- [24] S. Iihama, Y. Xu, M. Deb, G. Malinowski, M. Hehn, J. Gorchon, E. E. Fullerton, and S. Mangin, *Adv. Mater.* **30**, 1804004 (2018).
- [25] Q. Remy, J. Igarashi, S. Iihama, G. Malinowski, M. Hehn, J. Gorchon, J. Hohlfeld, S. Fukami, H. Ohno, and S. Mangin, *Adv. Sci.* **7**, 2001996 (2020).
- [26] D. Rudolf, C. La-o vorakiat, M. Battiato, R. Adam, J. M. Shaw, E. Turgut, P. Maldonado, S. Mathias, P. Grychtol, H. T. Nembach, T. J. Silva, M. Aeschlimann, H. C. Kapteyn, M. M. Murnane, C. M. Schneider, and P. M. Oppeneer, *Nat. Commun.* **3**, 1037 (2012).
- [27] A. Eschenlohr, L. Persichetti, T. Kachel, M. Gabureac, P. Gambardella, and C. Stamm, *J. Phys.: Condens. Matter* **29**, 384002 (2017).
- [28] F. Siegrist, J. A. Gessner, M. Osslander, C. Denker, Y.-P. Chang, M. C. Schröder, A. Guggenmos, Y. Cui, J. Walowski, U. Martens, J. K. Dewhurst, U. Kleineberg, M. Müntenberg, S. Sharma, and M. Schultze, *Nature (London)* **571**, 240 (2019).
- [29] I. Vaskivskiy, R. S. Malik, L. Salemi, D. Turenne, R. Knut, J. Brock, R. Stefanuik, J. Söderström, K. Carva, E. E. Fullerton, P. M. Oppeneer, O. Karis, and H. A. Dürr, *J. Phys. Chem. C* **125**, 11714 (2021).
- [30] M. Hennes, G. Lambert, V. Chardonnet, R. Delaunay, G. S. Chiuzbăian, E. Jal, and B. Vodungbo, *Appl. Phys. Lett.* **120**, 072408 (2022).
- [31] K. Carva, *Nat. Phys.* **10**, 552 (2014).
- [32] I. Razdolski, A. Alekhin, N. Ilin, J. P. Meyburg, V. Roddatis, D. Diesing, U. Bovensiepen, and A. Melnikov, *Nat. Commun.* **8**, 15007 (2017).
- [33] M. L. M. Laliu, R. Lavrijsen, R. A. Duine, and B. Koopmans, *Phys. Rev. B* **99**, 184439 (2019).
- [34] P. Baláž, M. Žonda, K. Carva, P. Maldonado, and P. M. Oppeneer, *J. Phys.: Condens. Matter* **30**, 115801 (2018).
- [35] M. L. M. Laliu, M. J. G. Peeters, S. R. R. Haenen, R. Lavrijsen, and B. Koopmans, *Phys. Rev. B* **96**, 220411(R) (2017).
- [36] H. Ulrichs and I. Razdolski, *Phys. Rev. B* **98**, 054429 (2018).
- [37] U. Ritzmann, P. Baláž, P. Maldonado, K. Carva, and P. M. Oppeneer, *Phys. Rev. B* **101**, 174427 (2020).
- [38] P. Baláž, K. Carva, U. Ritzmann, P. Maldonado, and P. M. Oppeneer, *Phys. Rev. B* **101**, 174418 (2020).
- [39] N. Berggaard, M. Hehn, K. Carva, P. Baláž, S. Mangin, and G. Malinowski, *Appl. Phys. Lett.* **117**, 222408 (2020).
- [40] M. Shalaby, A. Donges, K. Carva, R. Allenspach, P. M. Oppeneer, U. Nowak, and C. P. Hauri, *Phys. Rev. B* **98**, 014405 (2018).
- [41] M. Berritta, R. Mondal, K. Carva, and P. M. Oppeneer, *Phys. Rev. Lett.* **117**, 137203 (2016).
- [42] N. Kerber, D. Ksenzov, F. Freimuth, F. Capotondi, E. Pedersoli, I. Lopez-Quintas, B. Seng, J. Cramer, K. Litzius, D. Lacour, H. Zabel, Y. Mokrousov, M. Kläui, and C. Gutt, *Nat. Commun.* **11**, 6304 (2020).
- [43] S. Ghosh, A. Manchon, and J. Železný, *Phys. Rev. Lett.* **128**, 097702 (2022).
- [44] K. Xia, M. Zwierzycki, M. Talanana, P. J. Kelly, and G. E. W. Bauer, *Phys. Rev. B* **73**, 064420 (2006).
- [45] M. Zwierzycki, P. A. Khomyakov, A. A. Starikov, K. Xia, M. Talanana, P. X. Xu, V. M. Karpan, I. Marushchenko, I. Turek, G. E. W. Bauer, G. Brocks, and P. J. Kelly, *Physica Status Solidi B* **245**, 623 (2008).
- [46] J. Bass and W. P. Pratt, Jr., *J. Magn. Magn. Mater.* **200**, 274 (1999).
- [47] J. Bass and W. P. Pratt, Jr., *J. Phys.: Condens. Matter* **19**, 183201 (2007).
- [48] W.-T. Lu, Y. Zhao, M. Battiato, Y. Wu, and Z. Yuan, *Phys. Rev. B* **101**, 014435 (2020).
- [49] D. M. Nenno, S. Kaltenborn, and H. C. Schneider, *Phys. Rev. B* **94**, 115102 (2016).
- [50] D. M. Nenno, B. Rethfeld, and H. C. Schneider, *Phys. Rev. B* **98**, 224416 (2018).
- [51] V. P. Zhukov, E. V. Chulkov, and P. M. Echenique, *Phys. Rev. B* **72**, 155109 (2005).
- [52] V. P. Zhukov, E. V. Chulkov, and P. M. Echenique, *Phys. Rev. B* **73**, 125105 (2006).
- [53] M. Battiato, P. Maldonado, and P. M. Oppeneer, *J. Appl. Phys.* **115**, 172611 (2014).
- [54] V. P. Amin, P. M. Haney, and M. D. Stiles, *J. Appl. Phys.* **128**, 151101 (2020).
- [55] V. P. Zhukov, E. V. Chulkov, and P. M. Echenique, *Physica Status Solidi A* **205**, 1296 (2008).
- [56] M. Zwierzycki, Y. Tserkovnyak, P. J. Kelly, A. Brataas, and G. E. W. Bauer, *Phys. Rev. B* **71**, 064420 (2005).
- [57] O. K. Andersen, O. Jepsen, and D. Glötzel, in *Highlights of Condensed Matter Theory*, International School of Physics ‘Enrico Fermi’, Varenna, Italy, edited by F. Bassani, F. Fumi, and M. P. Tosi (North-Holland, Amsterdam, 1985), pp. 59–176.
- [58] I. Turek, V. Drchal, J. Kudrnovský, M. Šob, and P. Weinberger, *Electronic Structure of Disordered Alloys, Surfaces and Interfaces* (Kluwer, Boston-London-Dordrecht, 1997).
- [59] P. Baláž, M. Zwierzycki, and J. Barnaś, *Phys. Rev. B* **88**, 094422 (2013).
- [60] B. Koopmans, M. van Kampen, J. T. Kohlhepp, and W. J. M. de Jonge, *Phys. Rev. Lett.* **85**, 844 (2000).
- [61] I. A. Yastremsky, P. M. Oppeneer, and B. A. Ivanov, *Phys. Rev. B* **90**, 024409 (2014).
- [62] M. D. Stiles and A. Zangwill, *Phys. Rev. B* **66**, 014407 (2002).
- [63] A. Ghosh, S. Auffret, U. Ebels, and W. E. Bailey, *Phys. Rev. Lett.* **109**, 127202 (2012).
- [64] J. Barnaś, A. Fert, M. Gmitra, I. Weymann, and V. K. Dugaev, *Phys. Rev. B* **72**, 024426 (2005).